

RESEARCH ARTICLE

10.1002/2015JB011921

Key Points:

- Seismogeodetic data can provide rapid earthquake models
- Rupture is fast on a dipping strike-slip fault
- The surface trace is likely not the extension of the fault plane

Supporting Information:

- Text S1 and Figures S1–S10
- Animation S1

Correspondence to:

D. Melgar,
dmelgar@berkeley.edu

Citation:

Melgar, D., J. Geng, B. W. Crowell, J. S. Haase, Y. Bock, W. C. Hammond, and R. M. Allen (2015), Seismogeodesy of the 2014 M_w 6.1 Napa earthquake, California: Rapid response and modeling of fast rupture on a dipping strike-slip fault, *J. Geophys. Res. Solid Earth*, 120, 5013–5033, doi:10.1002/2015JB011921.

Received 29 JAN 2015

Accepted 19 MAY 2015

Accepted article online 25 MAY 2015

Published online 14 JUL 2015

Seismogeodesy of the 2014 M_w 6.1 Napa earthquake, California: Rapid response and modeling of fast rupture on a dipping strike-slip fault

Diego Melgar¹, Jianguhui Geng², Brendan W. Crowell³, Jennifer S. Haase², Yehuda Bock², William C. Hammond⁴, and Richard M. Allen¹

¹Seismological Laboratory, University of California, Berkeley, California, USA, ²Cecil H. and Ida M. Green Institute of Geophysics and Planetary Physics, Scripps Institution of Oceanography, University of California San Diego, La Jolla, California, USA, ³Department of Earth and Space Sciences, University of Washington, Seattle, Washington, USA, ⁴Nevada Geodetic Laboratory, University of Nevada, Reno, Reno, Nevada, USA

Abstract Real-time high-rate geodetic data have been shown to be useful for rapid earthquake response systems during medium to large events. The 2014 M_w 6.1 Napa, California earthquake is important because it provides an opportunity to study an event at the lower threshold of what can be detected with GPS. We show the results of GPS-only earthquake source products such as peak ground displacement magnitude scaling, centroid moment tensor (CMT) solution, and static slip inversion. We also highlight the retrospective real-time combination of GPS and strong motion data to produce seismogeodetic waveforms that have higher precision and longer period information than GPS-only or seismic-only measurements of ground motion. We show their utility for rapid kinematic slip inversion and conclude that it would have been possible, with current real-time infrastructure, to determine the basic features of the earthquake source. We supplement the analysis with strong motion data collected close to the source to obtain an improved postevent image of the source process. The model reveals unilateral fast propagation of slip to the north of the hypocenter with a delayed onset of shallow slip. The source model suggests that the multiple strands of observed surface rupture are controlled by the shallow soft sediments of Napa Valley and do not necessarily represent the intersection of the main faulting surface and the free surface. We conclude that the main dislocation plane is westward dipping and should intersect the surface to the east, either where the easternmost strand of surface rupture is observed or at the location where the West Napa fault has been mapped in the past.

1. Introduction

On 24 August 2014, an M_w 6.1 earthquake occurred 9 km south-southwest of the city of Napa, California. One fatality was reported, and damage to property and infrastructure was estimated to be in the 0.1 to 1 billion dollar range (<http://comcat.cr.usgs.gov/earthquakes/eventpage/nc72282711#pager>). The closest mapped fault to the event epicenter is the West Napa fault (WNF, Figure 1). The WNF is generally considered to be a San Andreas fault-parallel structure that dips to the west at 75° [Field *et al.*, 2014]. It has Quaternary displacement and is estimated to be 57 km long, extending northwest of San Pablo Bay [Wesling and Hanson, 2008]. Slip rate estimates incorporated into the California probabilistic hazards map are as low as 1 ± 1 mm/yr [Cao *et al.*, 2003]. However, these are poorly constrained because there have been few paleoseismic and geodetic studies of this tectonic structure. Unruh *et al.* [2002] suggested that a significant amount of slip is transferred from the Northern Calaveras fault (NCF) to the WNF, and d'Alessio *et al.* [2005] found, from GPS velocities, a slip rate of 4 ± 3 mm/yr. Indeed, because it has poor geomorphic expression, it is generally been assumed that the WNF is only accommodating small amounts of the plate boundary motion [Working Group on Northern California Earthquake Potential, 1996]. Seismicity rates are also low in the vicinity of the WNF [Waldhauser and Ellsworth, 2002]. Thus, current regional forecast models place slip at 1–4 mm/yr on this fault system [Field *et al.*, 2014]. Recent block modeling studies that incorporate interferometric synthetic aperture radar (InSAR) and GPS [Evans *et al.*, 2012] suggest a much higher slip rate of 9.5 ± 1.4 mm/yr, which is a significant portion of the total plate rate (~50 mm/yr) [DeMets *et al.*, 2009]. However, there is little evidence of significant large historical earthquakes. Recently, the 2000 M_w 5.0 Yountville earthquake ruptured in the Mayacamas Mountains, to the west of the WNF, between it and the Rodgers Creek fault (RCF). The only other large historic event in the area is the Mare Island earthquake

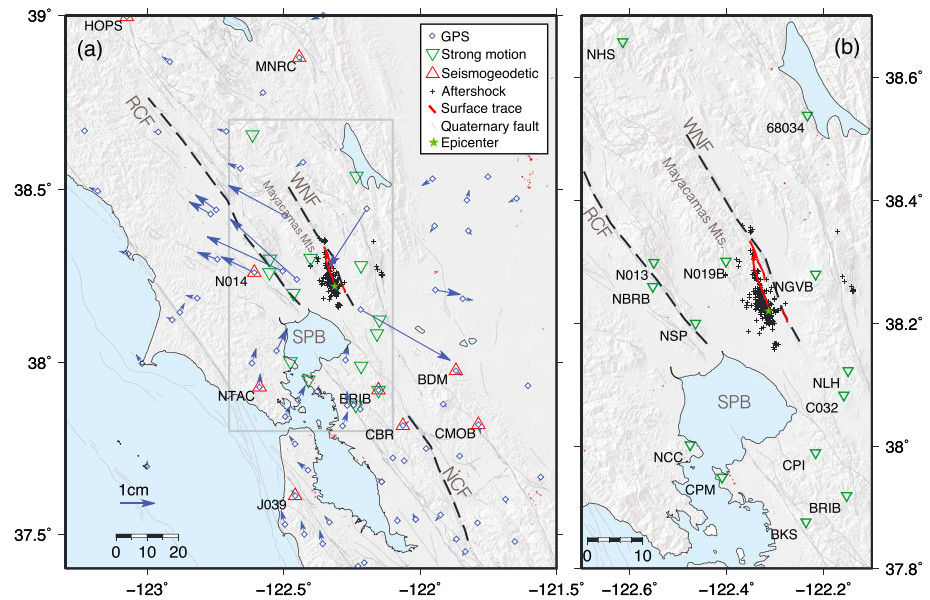


Figure 1. (a) Station distribution used for analysis of the earthquake source. Blue markers and arrows are the GPS stations and coseismic offsets produced from a postprocessed daily analysis of GPS displacements. Green triangles are 14 strong motion stations used for the final slip model. Red triangles are collocated GPS/strong motion stations used for rapid inversion. Also indicated is the surface trace of rupture, the epicenter, and 1 week of aftershocks. (b) Close up of the rectangular region marked in Figure 1a. Faults mentioned in the text are the West Napa fault (WNF), the Rodgers Creek fault (RCF), and the Northern Calaveras fault (NCF). SPB is San Pablo Bay.

sequence from 1886 to 1900. The main shock of this sequence has been estimated at $M_{6.2}$ and likely occurred on the southern terminus of the RCF [Toppozada et al., 1992] close to San Pablo bay.

The work that follows is conceptually divided into two parts. First, because of the location of the event, within the coverage area of real-time GPS networks, we will analyze in detail the potential contribution of the data for rapid response modeling of earthquake source parameters through peak ground displacement (PGD) scaling laws, a centroid moment tensor (CMT) solution, and a static slip inversion. We will further explore the real-time fusion of high-rate GPS data with strong motion data at collocated GPS/seismic stations. This *seismogeodetic* combination [Bock et al., 2011] is attractive for medium to large events because baseline offsets in strong motion data [Boore and Bommer, 2005] require corrections that make real-time use of medium- to long-period (roughly 10 s periods and longer) accelerometer time series unreliable [Melgar et al., 2013a]. Low-pass filtering accelerometer data require the assumption that the event is small enough to safely neglect long-period information. This assumption cannot be made when designing a robust warning and rapid response system that must function for the maximum size event. We will show how this sensor combination can be employed to produce broadband strong motion displacement and velocity waveforms, how it falls short in the rapid determination of the kinematic features of this particular earthquake source, and what must be done to realize the full potential of this method.

Second, we produce a postprocessed kinematic model that incorporates, in addition to the seismogeodetic data, corrected accelerometer time series close to the event which are difficult to employ by themselves in real time, as well as postprocessed estimates of coseismic offsets at GPS stations in the region. We find that rupture is best described by fast (near shear speed) unilateral propagation on a subvertical westward dipping fault plane. Notably, there is significant surface expression of the rupture in the flat low-lying agricultural areas of the southern portion of Napa valley (Figure 1). The surface break is roughly divided into eastern and western strands in the south that coalesce into a single strand in the north [Beyzaei et al., 2014]. Several smaller surface fractures have been reported as well. We present a detailed analysis of the kinematic characteristics of the earthquake that with knowledge of the local geology offers a potential explanation for the apparent complexity of the surficial features. Furthermore, we test whether the fault plane we derive from geodetic data intersects the surface where rupture has been documented.

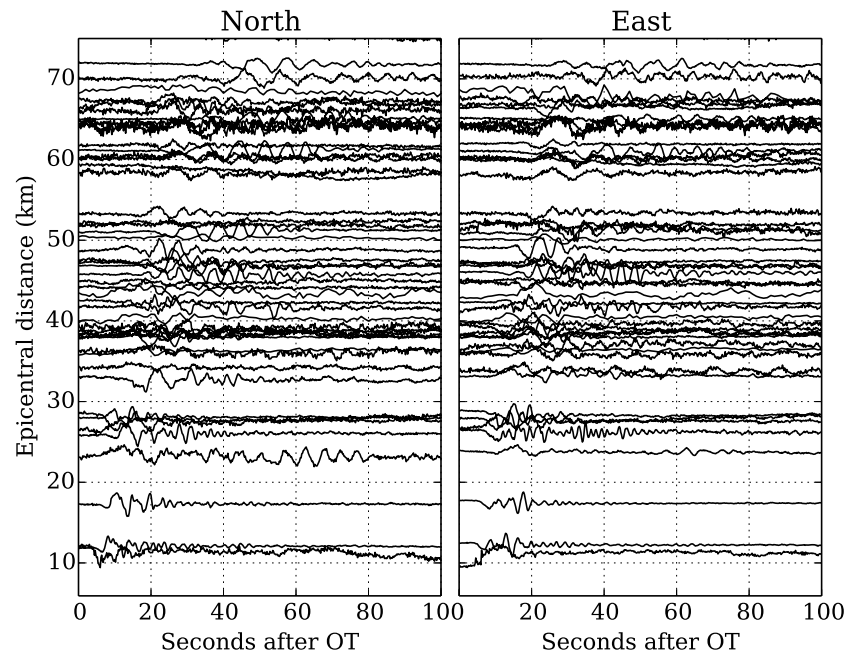


Figure 2. Record section of high-rate GPS displacement waveforms within 75 km of the event epicenter.

2. Data

We analyze high rate as well as 24 h Global Positioning System (GPS) position data. GPS recordings are from the Plate Boundary Observatory (PBO) and Bay Area Regional Deformation (BARD) networks. High-rate GPS positions (Figure 2) are computed at 1–5 Hz depending on a station's sampling rate. We use precise point positioning with ambiguity resolution (PPP-AR) to achieve real-time centimeter-level precision [Ge *et al.*, 2008; Geng *et al.*, 2013]. With the PPP-AR approach, no nearby (e.g., within tens of kilometers) reference stations are required, and absolute positions relative to a global reference frame are efficiently generated on a station-by-station basis, rather than by regional relative positions ("baselines") [e.g., Crowell *et al.*, 2009; Grapenthin *et al.*, 2014a]. Comparable positioning precision to that of relative positioning is achieved. As part of the real-time operational infrastructure at the Scripps Orbit and Permanent Array Center, International Global Navigation Satellite Systems Service predicted ultrarapid orbits to estimate 1 Hz satellite clock products, and 0.2 Hz satellite fractional-cycle bias (FCB) products based on a network of 66 reference stations are used as described by Geng *et al.* [2013]. This network stretches from the central U.S. to Hawaii, Canada, and South America and is designed to provide FCB products for ambiguity resolution for any earthquake location on the West Coast of the U.S., which are robust to any contamination from ground motion at stations within the zone of interest. Using the real-time satellite products described above, we retrospectively analyzed real-time PPP-AR positions at 31 5 Hz stations from the Bay Area Regional Deformation Network (BARD) and 183 5 Hz stations from the Plate Boundary Observatory (PBO) which are all located within 300 km of the Napa Valley. After successful ambiguity resolution and for sites not subject to local multipath, the positioning precision is typically better than 1 cm in the horizontal components and about 3 cm in the vertical component [Geng *et al.*, 2011, 2013]. We extract coseismic static offsets from this high-rate displacement data (henceforth referred to as rapid offsets and available within 50 s of origin time) with a moving median filter and trailing variance approach where the time of the static offset is selected to be greater than the time where variance drops to 25% of the maximum variance [Melgar *et al.*, 2012] (Figure 3). For postprocessed slip models, we employ static offsets from the 30 s sampled 24 h GPS solutions computed at 147 stations in the region (henceforth referred to as postprocessed offsets, Figure 1). These were computed with the GIPSY/OASIS-II software at the Nevada Geodetic Laboratory.

We employ strong motion data from three local networks, the Northern California Seismic Network (NC), the California Strong Motion Instrumentation Program network (CE), and the Berkeley Seismic Network (BK).

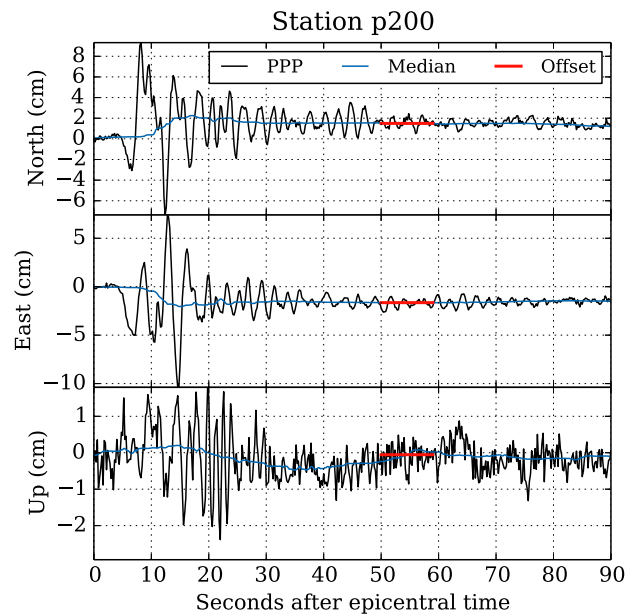


Figure 3. Example application of the moving median filter technique to rapidly estimate coseismic displacement. The blue line is the 10 s moving median filter, and the red line is the data segment identified for averaging and offset determination.

[2014] that simultaneously solves for an accelerometer bias that is slowly varying in time. The seismogeodetic time series do not require band-pass filtering. This is a distinct advantage over high-pass filtered accelerometer data to remove systematic effects (baseline offsets). GPS data have higher-noise levels than seismic data, especially in the vertical component, and slow sampling rates can introduce aliasing [Smalley, 2009], thus the seismogeodetic combination includes the most reliable aspects of both data sets.

Seismogeodetic data are preferable for any real-time source computation because they mitigate systematic errors typically afflicting both sensor types. However, seismic and geodetic networks have developed independently, and collocations are few, in this case only nine within 75 km with a poor azimuthal distribution. For the postprocessed kinematic slip inversion, we augment the stations used for source analysis with 13 additional strong motion-only sites (Figure 1) that are located close to the earthquake and with favorable azimuthal coverage of the event. These sites are classified as NEHRP class B/C conditions (v_{s30} of 760 m/s) where possible on the north side of the event, however, only site class C ($v_s > 360$ m/s) was available south of the event (Figure 4). These are sites characterized as being on soft rock or harder surface [Holzer et al., 2005]. This ensures that site effects do not overly affect the data. Geologically or geotechnically derived site condition information does not exist for all of the strong motion sites in the western U.S.; we rely on v_{s30} estimates from terrain gradient as a proxy [Allen and Wald, 2009].

3. Source Analysis Methods

We present the results from several source modeling algorithms with increasing levels of complexity which are described in this section. We begin with peak ground displacement (PGD) scaling that produces only a magnitude estimate. We then discuss algorithms that use GPS static offsets, a centroid moment tensor (CMT) calculation that indicates the style of faulting followed by a static inversion on the CMT nodal planes. Finally, we discuss time-dependent models from a kinematic slip inversion that uses geodetic, seismic, and seismogeodetic data.

3.1. Peak Ground Displacement Scaling

Rapid magnitude estimates as a function of time elapsed since the start of rupture can be readily obtained from the high-rate GPS data by measurement of the peak ground displacement (PGD). Crowell et al. [2013]

To estimate seismogeodetic waveforms, we use data from nine strong motion stations that are collocated with GPS stations. We consider sites to be collocated when they are separated by less than 1 km. Simple gain response is removed from the strong motion data and they are combined with the high-rate GPS data using a multirate Kalman filter [Bock et al., 2011]. This analysis produces broadband seismogeodetic velocity and displacement waveforms (Figure S1 in the supporting information) at the sample rate of the accelerometer (100–200 Hz). Objective estimates of the Kalman filter variances, critical to the filter performance, are obtained from 60 s of preevent noise on both seismic and geodetic sensors. The zero baseline, or DC offset, of real-time strong motion data is typically removed in postprocessing. In our real-time formulation, the DC offset is automatically removed by employing the augmented filter formulation of Melgar

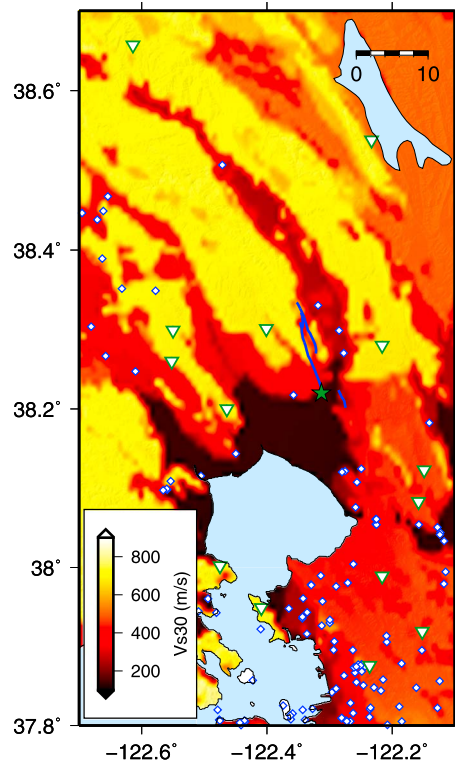


Figure 4. Values of v_{s30} determined from terrain slope as in *Allen and Wald [2009]* used to select a subset of strong motion stations for the inversion.

we invert for the centroid moment tensor using the inversion and grid search approach of *Melgar et al. [2012] (fastCMT)*. We assume a 1-D layered Earth structure model (GIL7) calibrated for the San Francisco Bay area and used in regional moment tensor inversion [*Dreger and Romanowicz, 1994*]. Static Green's Functions (GFs) are computed for this structure with EDGRN [*Wang et al., 2003*]. This code relies on the closed form solutions of the partial differential equations of motion obtained from the Hankel transform and then applies a Thomson-Haskell propagator matrix to relate the deformation at depth with that at the surface. In order to test the reliability of the rapid CMT computation, we produce two different solutions, the first is obtained using the rapid offsets extracted from the high-rate data (Figure 3); the second solution is computed from the postprocessed static offsets. We expect the rapid offsets are noisier than the postprocessed ones, although the latter could include early afterslip. Then from the moment tensor, we extract the two possible nodal planes from the best double couple and use them as the dislocation surface for a static slip inversion [*Crowell et al., 2012; Melgar et al., 2013b*]. While the static inversions do not contain information on the time behavior of rupture, the total slip that is retrieved provides a good estimate of the spatial extent of the earthquake rupture, and they are computationally simple because they have no temporal dependence and thus are suitable for rapid computation.

3.3. Kinematic Source Models

A more complex description that includes the time-dependent behavior of rupture is important because it can describe the velocity pulses and rupture directivity that produce anomalously high ground motions, which can potentially create regions of localized damage [*Dreger and Kaverina, 2000*]. For our rapid computation, we jointly invert the seismogeodetic displacement and velocity waveforms to estimate a kinematic slip model. As remarked upon earlier, this affords several advantages over seismic only or geodetic-only kinematic inversions. For automated rapid computation, no band-pass filtering is necessary, so the seismogeodetic waveforms can be ingested directly into the inverse code without any ad hoc corrections. Furthermore, *Melgar and Bock [2015]* showed that the simultaneous inversion of displacement and velocity data results in a kinematic model that is reliable across a wider frequency band. Displacement

derived, from seismogeodetic recordings of earthquakes of moment magnitude 5 to 9, the following scaling law relating the observed PGD distribution to the magnitude of an event:

$$\log(\text{PGD}) = -5.013 + 1.219M_w - 0.178M_w \log(R), \quad (1)$$

where R is the distance from the station to the source. We test this PGD regression here by applying it to the high-rate GPS displacement data for stations where PGD is larger than 2 cm. This threshold is selected to ensure we employ only stations where the signal is significantly above the accuracy level of GPS-only data and comparable to the seismogeodetic value of PGD. The earthquake location and origin time are fixed to the values determined by the regional seismic early warning system [*Bose et al., 2014*], with the depth set to 8 km. We apply a 1.5 km/s traveltime mask, and PGD derived magnitude estimates are only given after four stations have reported a measurement.

3.2. Static Source Models

We estimate a more complex model using the coseismic offsets that represent the static deformation field. From the rapid GPS offsets,

data constrain lower frequency behavior while velocity data are sensitive to higher frequency features. The result of this kinematic slip inversion is analogous to what could be available in real time and can be compared to the more accurate postprocessed model.

The seismogeodetic collocations are few and not as close to the event as would be desirable. Thus, for a more detailed, postprocessed model, we add 13 extra three-component strong motion stations along with the postprocessed static offset estimates (Figure 1) to the inversion process. The strong motion data are integrated to velocity and band-pass filtered between 20 s and 2 s period to remove baseline offsets. This choice of frequency band and integration to velocity rather than displacement is based on an analysis of the biases introduced by baseline offsets shown in the results section. This determination is difficult in real time and is restricted to postevent analyses.

To solve for the distribution of slip from the time series, for both rapid and postprocessed kinematic inversions, we use the multitime window approach [Ide *et al.*, 1996]. We employ a 1×1 km subfault discretization of the nodal plane from the moment tensor inversion. The fault plane extends from the surface to 15 km depth. Complete GFs are computed with the frequency wave number technique of Zhu and Rivera [2002]. The velocity structure is the GIL7 model, as in the static case. We use a maximum rupture speed of 3 km/s, corresponding to 0.9 times the shear wave speed of the highest velocity layer spanned by the fault model. We use triangle-shaped source time functions with 0.333 s rise times. Slip is allowed on fifteen 50% overlapping windows. This does not force propagation at 3 km/s but rather is the fastest rupture velocity allowed in the inversion. A useful rule of thumb is to choose the fault size such that the number of parameters is computationally tractable (usually 100–500 subfaults) and the rise time to be roughly the time it takes the rupture front to cross the subfault at the given maximum rupture speed. Since kinematic inversion is an ill-conditioned problem, we employ first derivative temporal regularization on the slip windows and Laplacian regularization on the total slip at each subfault [Wu *et al.*, 2001]. The regularization parameters are determined objectively, without analyst interaction through Akaike's Bayesian Information Criterion formalism (ABIC) [Fukahata *et al.*, 2003].

4. Results

We present the results in the chronological order in which they are available and utilized and as they were introduced in section 3. First, we discuss PGD scaling and then static offset estimation from the high-rate GPS data followed by CMT and static slip inversion. We then present the results for the simulated real-time seismogeodetic waveform calculation and its utility for rapid kinematic slip inversion. Note that the seismogeodetic data could also be used to derive reliable estimates of PGD magnitude and the CMT if there were a larger number of collocated sites available. Finally, we present the postprocessed kinematic model that includes the seismogeodetic data and post hoc corrected strong motion sites close to the event. We discuss the relationship between the modeled rupture kinematics and the observed surface rupture, based on the postprocessed solution.

4.1. PGD-Derived Magnitudes

The time evolution of moment magnitude estimates from GPS peak ground displacements measured at stations within 75 km of the event is shown in Figure 5a. For comparison, note that the ShakeAlert early warning system issued a M_w 5.7 alert 5 s after origin time [Grapenthin *et al.*, 2014a, 2014b], the Berkeley automated full waveform moment tensor solution for this event had M_w 6.0 and the USGS W-phase solution M_w 6.1, both \sim 10 min after origin time (both solutions can be found at <http://earthquakes.usgs.gov>). Recall that for a magnitude estimate to be made, we require at least four stations to report a PGD measurement. At 17 s after origin time (OT) with four stations, the magnitude estimate is M_w 5.55. By 20 s with 12 stations, the estimate increases to M_w 5.7. The estimate reaches M_w 5.9 by 35 s, M_w 6.0 at 45 s, and stabilizes after 50 s at M_w 6.05.

The initial estimate was made using the scaling law derived from a set of seven earthquakes [Crowell *et al.*, 2013]. The estimate is well within the magnitude error bars reported for the relation. As more events such as the Napa earthquake are added to the PGD catalog, the scaling law should improve. We updated the

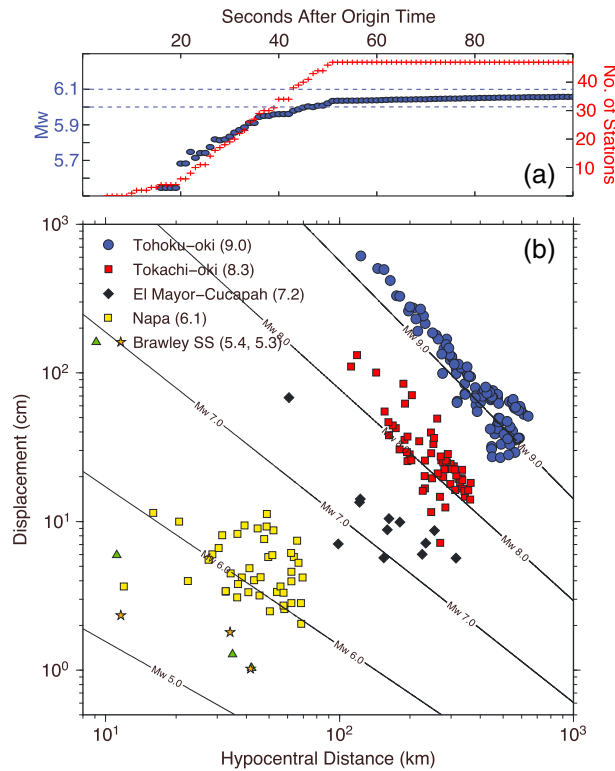


Figure 5. (a) Temporal evolution of magnitude determination from peak ground displacement (PGD) measurements. The red crosses indicate the number of stations used in the regression. (b) Data points [Crowell *et al.*, 2013] used to determine the original regression and the measurements for the Napa event.

scaling law with the observations from the Napa earthquake. (Figure 5b). With inclusion of the Napa data set, the regression law slightly changes to

$$\log(\text{PGD}) = -4.508 + 1.129M_w - 0.165M_w \log(R). \quad (2)$$

4.2. Static Offset Estimation

We employ two static offset data sets (both from GPS-only data), the rapid offsets from the high-rate data and the postprocessed offsets from the 24 h solutions. Both are used for CMT computation (Figures 6 and 7) and for the static slip inversion. Figure 3 shows an example of the moving median technique for extracting rapid static offsets from the high-rate GPS data for PBO station P200. The moving median of the time series stabilizes at ~20 s after OT within the arrival of the first surface wave oscillations. However, to be conservative, we delayed the final offset determination by 30 s to ensure that shaking has ceased and is not contaminating offset determination [Melgar *et al.*, 2012]. For P200, this occurs 50 s after OT. In California, instantaneous (1 Hz) GPS positions typically have horizontal noise levels of 10–20 mm

[Genrich and Bock, 2006; Geng *et al.*, 2013]; and therefore, many of the smaller rapid offsets are not above the noise level.

The static offsets estimated from the daily position estimates have higher signal to noise than the rapid offsets (Figure 6a). The postprocessed offsets were estimated from daily position solutions as the difference between the mean of 30 days of station positions before the event and data up to the end of a full day after the earthquake. The largest measured offset occurs at station P261 southeast of the epicenter with 29.6 ± 3.3 mm of horizontal motion. The postprocessed daily offsets rely on averaging over 24 h intervals and result in a single position for each day. This results in a mitigation of error sources that have period near 1 day, and thus have significantly lower noise levels and can better measure smaller coseismic motions.

4.3. Moment Tensor Solutions

In order to test the reliability of the static offset derived moment tensor computation at low magnitudes, we compare the solutions and centroid locations derived from the rapid and the postprocessed offsets. Using a grid search approach, the *fastCMT* solution [Melgar *et al.*, 2012] using the rapidly-estimated offsets can be obtained without an a priori earthquake location. They are potentially independent of the seismic network products and thus can serve as verification, and they do not contain additional latency from the seismic network-derived products. For this event, with a poor collocated station distribution, the results illustrate the tradeoff between speed and quality. The results are shown in Figures 6b and 7. Figure 7a shows the *fastCMT* solution constrained to the epicentral location determined by the seismic network. It has a low magnitude (M_w 5.6) and has low variance reduction (40%). Figure 7b is the solution after grid searching for the best possible centroid location. The magnitude increases to M_w 6.1 closer to the final value but the fits to the data remain poor (VR is 48%). Furthermore, the centroid is mislocated 10 km southwest of the source area. For both of these cases, the MT has a significant dip-slip component and a high-compensated

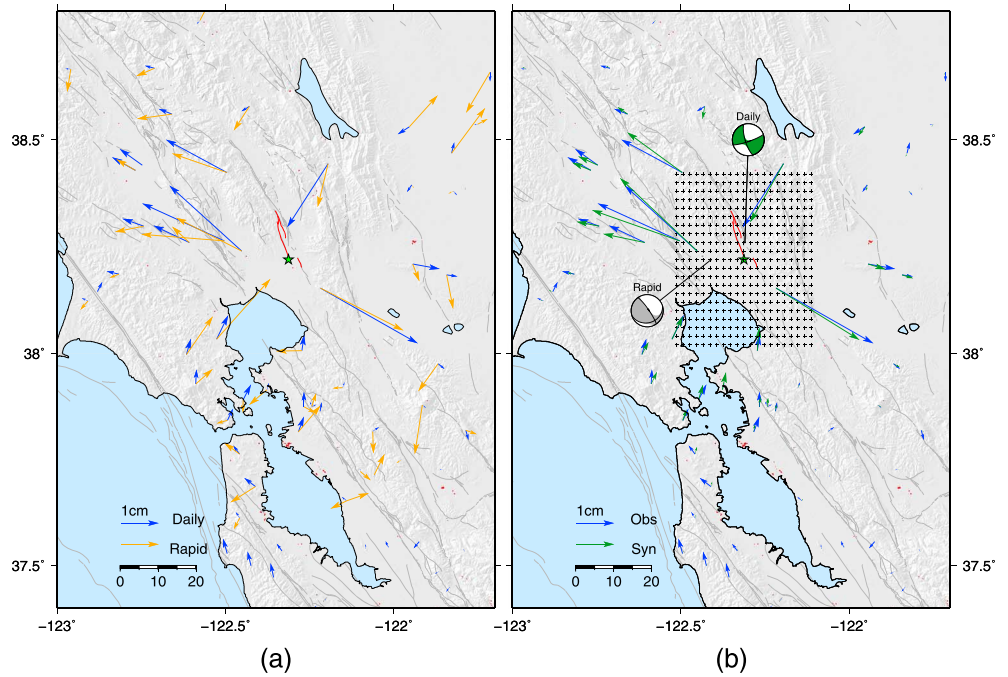


Figure 6. (a) Comparison of coseismic offsets determined from the daily GPS displacement time series and by the rapid technique using the high-rate data. (b) CMT solutions using the postprocessed and rapid offsets. Shown are the fits of the postprocessed model solution (green) to the observed offsets (blue). The grid of crosses is the locations that were used to search for the best fitting centroid.

linear vector dipole component. This is indicative of a poor solution for a tectonic earthquake, although one of the nodal planes still has a San Andreas fault-parallel subvertical geometry. These solutions are available as soon as static offsets are computed (50 s after OT). The CMT is derived from the more precise postprocessed daily offset data, and allowing for a grid search of the centroid location is much improved. It is located beneath the observed surface traces at a depth of 4 km. Its mechanism indicates right-lateral strike-slip motion on a subvertical westward dipping fault. The strike of the preferred nodal plane is parallel to the proposed

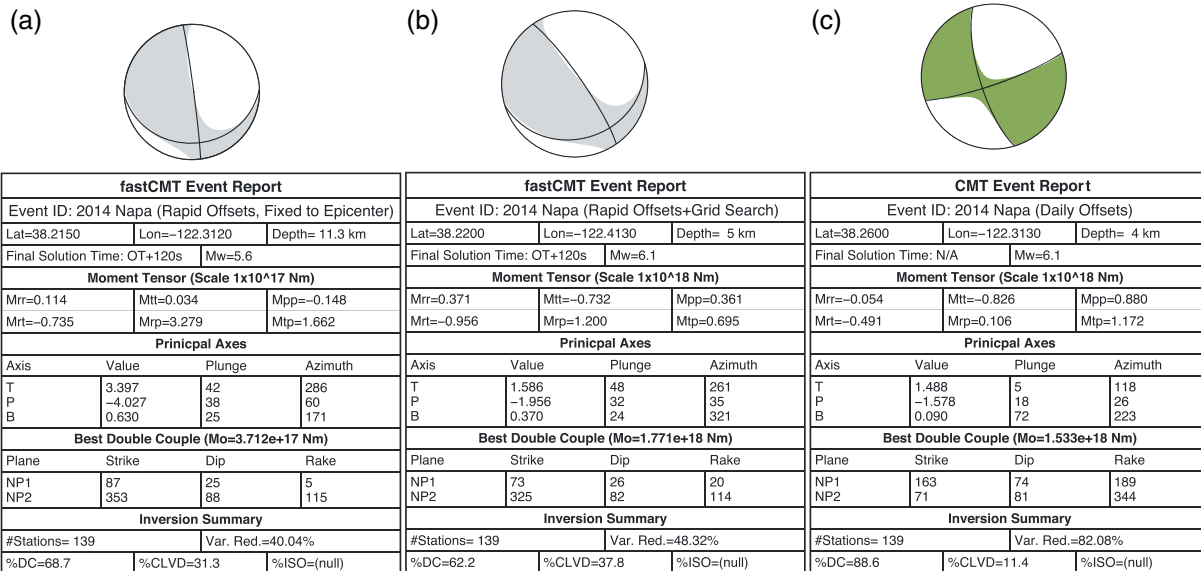


Figure 7. Moment tensor solutions. (a) Using the rapid offsets derived from the high-rate GPS data constraining the solution to the hypocenter. (b) Using the rapid offsets and allowing a grid search for the centroid. (c) Using the offsets derived from the daily GPS solutions and allowing a grid search for the centroid.

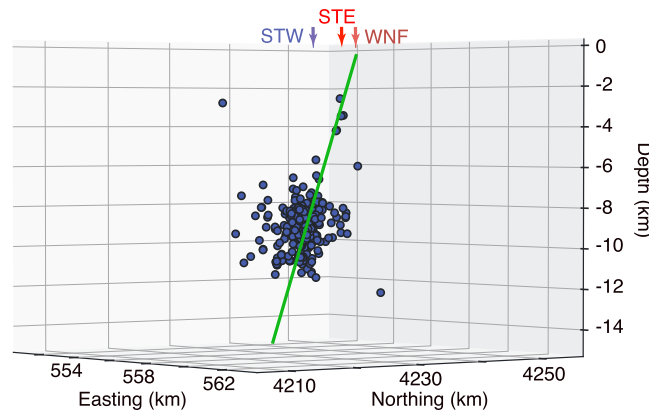


Figure 8. Perspective view of the nodal plane (NP1) from Figure 7c and its relation to the double difference relocated aftershocks. STW is the western strand of the surface trace, STE is the eastern strand (Figure 1), and WNF is the proposed location of the West Napa fault according to the UCERF3 model and the approximate location of the eastern strand of surface rupture.

determine the reliability for events at the lower magnitude limit. From the moment tensor solutions, we extract the two nodal planes and use the offset data to determine the appropriate fault plane by selecting, after static inversion on each plane, the one with better fit to the data. For the rapid computation, we use the nodal planes from the rapid moment tensor fixed to the epicenter (Figure 7a), and for the postprocessed one, we use the nodal planes from the postprocessed CMT solution (Figure 7c). The postprocessed fault plane indicates a southeast striking and westward dipping subvertical fault, which agrees well with double

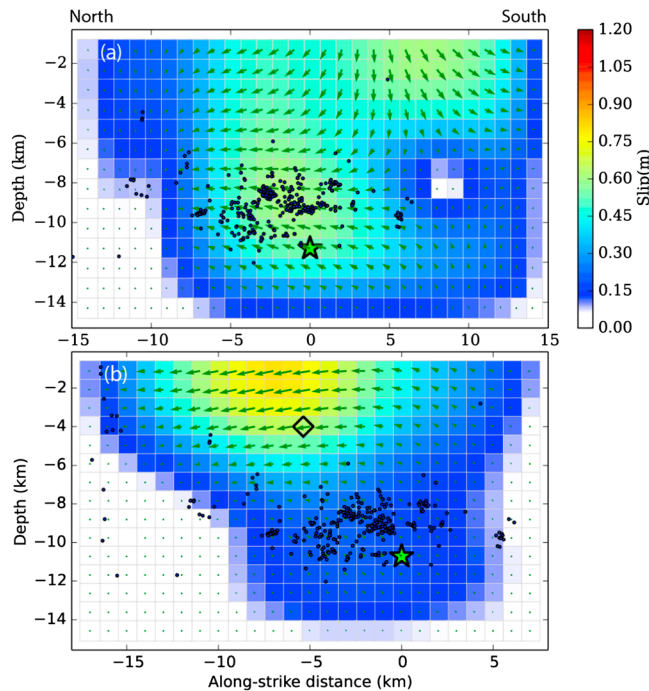


Figure 9. Static slip inversions of the earthquake. (a) Using the nodal plane from the rapid CMT solution (Figure 7a) (b) Using the nodal plane from the postprocessed CMT solution (Figure 7c). The green star denotes the hypocenter. The black diamond is the location of the centroid computed from the postprocessed CMT inversion (Figure 7c). Black circles are the double difference relocated aftershocks.

geometry of the WNF according to the Uniform California Earthquake Rupture Forecast, Version 3 (UCERF3) model [Field *et al.*, 2014] and with a very similar dip (74° versus 75° in UCERF3) and has a magnitude of M_w 6.1 with a variance reduction of 82%. In short, this mechanism is consistent with regional tectonics. Given the size of the offsets, the solution with more precise postprocessed data is more reliable than with rapid offsets.

4.4. Static Slip Inversion

We test the quality of a static slip inversion derived from the rapid offsets as compared to that obtained from the postprocessed ones to determine the reliability for events at the lower magnitude limit. From the moment tensor solutions, we extract the two nodal planes and use the offset data to determine the appropriate fault plane by selecting, after static inversion on each plane, the one with better fit to the data. For the rapid computation, we use the nodal planes from the rapid moment tensor fixed to the epicenter (Figure 7a), and for the postprocessed one, we use the nodal planes from the postprocessed CMT solution (Figure 7c). The postprocessed fault plane intersects the surface close to the proposed UCERF3 location of the surface expression of the WNF [Field *et al.*, 2014].

Figures 9a and 9b show the results of the rapid static slip inversions. Given that there is a significant dip-slip component in the rapid moment tensor solution (Figure 7a), we have not imposed any constraints in the direction of slip for the rapid static inversion (Figure 9a). This is to replicate the real-time scenario where no information on slip constraints is available. The maximum length of the fault plane is determined from the scaling relationships of Wells and Coppersmith [1994] using M_w 5.6 and then doubling that length to allow for perfectly unilateral rupture in either direction. The rapid inversion (Figure 9a) has peak slip of 0.7 m, total moment of 1.72×10^{19} Nm (M_w 6.1), and shows bilateral rupture with right-lateral strike-slip motion north of the hypocenter. To the south, rupture has significant oblique normal slip

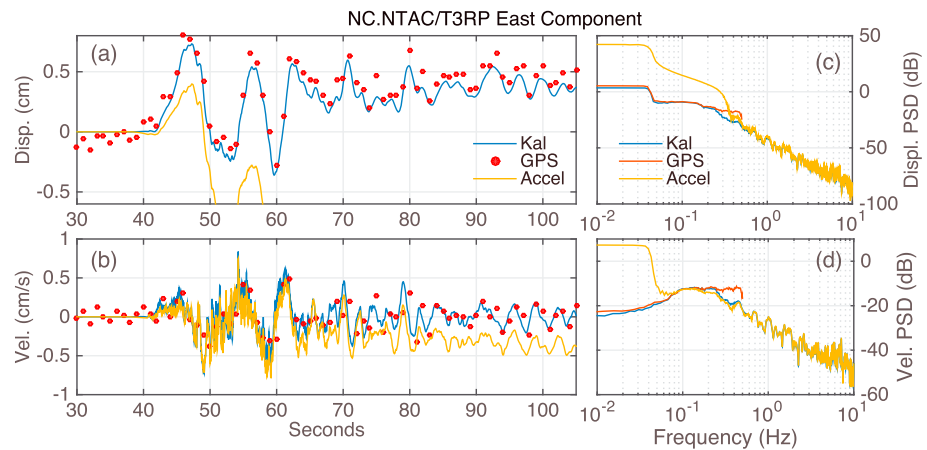


Figure 10. Example Kalman filtered waveform for accelerometer/GPS pair NC.NTAC/T3RP. (a) The seismogeodetic displacement compared to the high-rate GPS positions and the double integration of the zeroth order corrected accelerometer data. (b) The seismogeodetic velocity compared to the singly integrated zeroth order corrected accelerometer data and the first derivative of the GPS positions. (c and d) The multitaper power spectral densities for the displacement and velocity waveforms, respectively.

consistent with the rapid moment tensor solution of Figure 7a. There is slight left-lateral motion in the southern subfaults; this violates the nonnegativity assumption typically used in slip inversions. The postprocessed solution (Figure 9b) shows a smooth slip distribution with two broad regions of slip. Note that the dimensions of the fault surface assumed are smaller than in the rapid case. There is one area around the hypocenter with ~15 cm of slip and a shallower asperity ~15 km long between 6 km depth and the surface and with slip between ~50 cm and its peak slip of 80 cm. Total moment for this model of 1.82×10^{19} Nm (M_w 6.11) and the fits to the observed offsets are good (93% variance reduction). Slip in this model has been constrained to rake angles between 45° and 135° , consistent with right-lateral rupture and the postprocessed CMT inversion (Figure 7c). Since we know from the postprocessed MT that it has a right-lateral rupture, and to further stabilize the inversion, we include the nonnegativity constraint. While this is clearly a smooth representation of the source that smears many details of the rupture, broad features can be discerned. The model indicates a preferential propagation of slip to the north of the hypocenter and at depths shallower than 6–7 km. In addition, the location of the centroid derived from the postprocessed daily static offsets compares favorably to the locus of mean moment release in the static slip model. In summary, while the *fast*CMT solution is not exact because of higher-noise levels in the observations, it does recover the correct nodal plane of the rupture, retrieves approximately the amount of slip, and indicates the extension of slip toward the surface.

4.5. Seismogeodetic Time Series

As mentioned in section 1, real-time combination of strong motion and geodetic data has important applications to real-time seismology. We produce seismogeodetic displacement and velocity time series with the Kalman filter and smoother described in *Bock et al.* [2011]. To reduce noise as much as possible, in addition to the forward Kalman-filtering step, we employ a 5 s backward smoothing filter. To evaluate the improvement in source inversions over using the individual data sets, we estimate seismogeodetic waveforms for nine collocated strong motion/GPS sites surrounding the earthquake (Figure 1a). As for previous events where seismogeodetic time series have been analyzed [*Melgar et al.*, 2013b; *Geng et al.*, 2013], we retrospectively process the GPS data in simulated real-time mode. We extract the noise parameters (variance of the GPS solution) necessary for the filter from 60 s of preevent data. A sample of the displacement and velocity time series is shown in Figures 10a and 10b along with the corresponding power spectral densities in Figures 10c and 10d. The figure shows previously observed features of the Kalman filter remarked upon in detail in *Bock et al.* [2011] and *Melgar et al.* [2013a]. Namely, at long periods, the spectrum of the Kalman filter time series follows that of the GPS positions while at higher frequencies the spectrum follows that of the accelerometer. Figure 10 shows the power spectral density (PSD) of single and double integration of the zeroth order corrected (preevent mean removed) accelerometer time series. Recall from basic Fourier transform properties

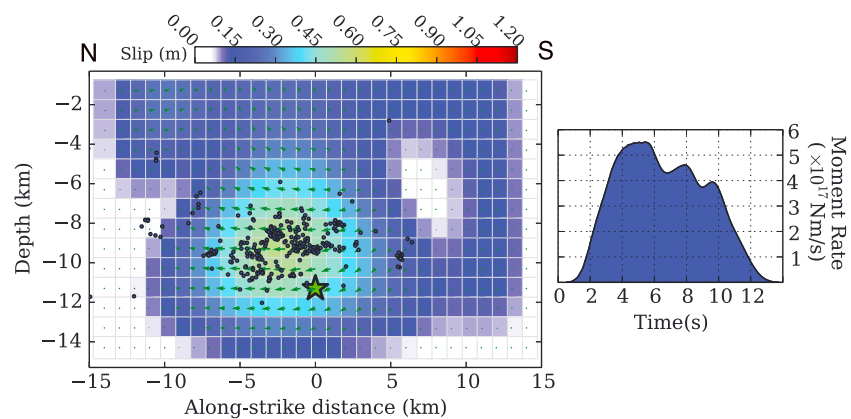


Figure 11. Slip distribution of the kinematic inversion of nine 3-component seismogeodetic stations. The green star denotes the hypocenter. Black circles are the double difference relocated aftershocks. Shown as well is moment release as a function of time for the event.

that every instance of integration is akin to dividing the PSD by f^2 where f is frequency. Thus, long-period noise is far more obvious in the displacements derived from double integration of acceleration data. For this same reason, velocities obtained by differentiating the GPS positions (equivalent to multiplying the PSD by a factor of f^2) show even higher levels of noise at high frequencies. The PSD plots not only describe the behavior of the filter but also, more importantly, illustrate that in the absence of collocated sites, if one is to rely on strong motion data for seismological analysis, and if baseline offsets are a concern, it is best to forego double integration and model instead with velocity time series. Figures 10c and 10d illustrates how the frequency domain biases of the integration of strong motion data extend to higher frequencies with displacement data than with velocity data. Baseline afflicted records have a broader bandwidth of reliability when analyzed as velocity. For the particular example in Figure 10, the doubly integrated displacement data show significant frequency domain errors at frequencies as high as ~ 0.4 Hz. In contrast, the velocity time series appears to be reliable down to periods of ~ 20 s. As noted in *Melgar et al.* [2013a], there is heterogeneity between stations and data directional components (channels) as to what portions of the spectrum are well captured by the accelerometer. Without external data, it is difficult to assess a priori the frequency band at which a particular site will be reliable. This will be important when we produce a final model of the earthquake source.

4.6. Kinematic Slip Inversion

It is of interest for rapid response to produce kinematic source models derived from these data since the seismogeodetic combination reduces the noise level of the displacement and velocity time series. Using the fault plane from the rapid moment tensor solution (Figure 7a), we perform a kinematic slip inversion of the event using data (Figure S1) from the nine collocated sites. Figure 11 shows the final slip distribution and source time function. The source duration is long (~ 12 s), and moment release happens smoothly over the duration of rupture. Total moment is higher than in the static case at 4.49×10^{19} Nm ($M_w 6.3$). The slip inversion result contains a main 10 km long asperity north of the hypocenter between 6 and 13 km depth with slip between ~ 15 cm and 50 cm. There is also subtle shallow patch of higher slip (~ 20 cm) to the north between 4 km and the surface. As with the static case, we have not placed any restrictions on the allowed rake directions. Nonetheless, and in contrast to the GPS-only static solution that had significant dip slip, the model shows almost exclusively right lateral motion. The fits to the data are moderate (VR is 52%, Figure S1) for both the seismogeodetic velocity and displacement time series.

To obtain a better image of the source process, we supplement the 9 seismogeodetic sites with 13 postprocessed strong motion sites (Figure 1b) and all of the postprocessed coseismic offsets. This improves the azimuthal coverage and adds stations that are closer to the event than the available seismogeodetic stations. To minimize site effects, the 13 additional sites are selected from all strong motion stations in the region because they have at least class B or C site conditions (Figure 4). Additionally, based on the frequency domain analysis of section 4.5 (Figure 10), we invert the strong motion data as velocity and band-pass filter the data between 20 s and 2 s. All data sets are equally

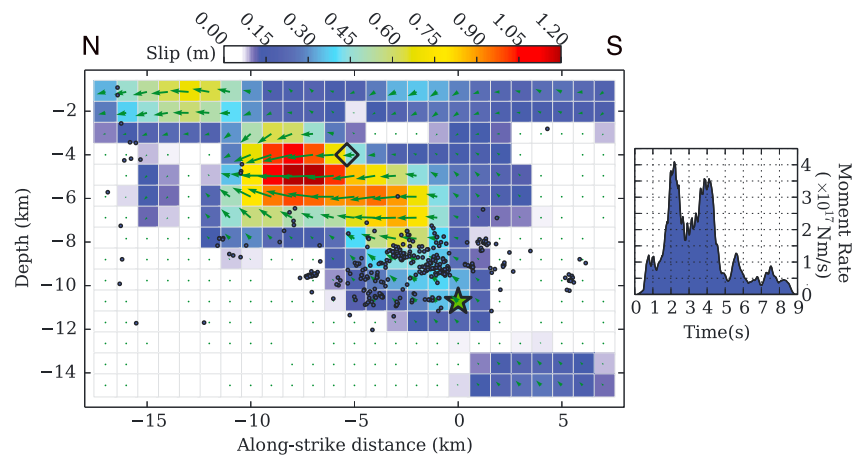


Figure 12. Slip distribution of the joint kinematic inversion of the nine seismogeodetic stations, 13 three-component strong motion stations, and daily coseismic offsets. The green star denotes the hypocenter. The black diamond is the location of the centroid computed from the CMT inversion (7c). Black circles are the double difference relocated aftershocks. Moment release as a function of time for the event is shown at right.

weighted in the inversion. We use the nodal planes from the postprocessed moment tensor (Figure 7c) for this inversion. As before, we retain the nodal plane that has the best fit to the data.

The final slip distribution from this joint inversion is shown in Figure 12. The total moment is 1.85×10^{19} Nm ($M_w 6.11$). Most of the slip in this model is concentrated updip and to the north of the hypocenter. Peak slip is 121 cm and motion is predominantly right-lateral with only a minor dip-slip component. There is an abundant shallow slip of the order of 60 cm along a 5 km long segment to the north and a small amount (~ 10 cm) to the south. Downdip and to the south of the hypocenter, there is a small 5 km long patch with ~ 15 cm of slip. Fits to the data are good with a variance reduction of 70% (Figure S1), and notably, significantly better than those for the seismogeodetic source inversion, for example, station MNRC. Stations to the north show systematically better fits than stations to the south. The peak velocities are well modeled at most stations.

The total duration of rupture is ~ 9 s (Figure 12); this is shorter than the 12 s rupture duration of the rapid model (Figure 11), and most of the moment release occurs within 5 s of rupture initiation. There are two pulses of slip in the source time function at around 2 s and 4 s. They correspond to large slip rates (Figures 13 and 14) in the subfaults of the main asperity updip and to the north of the hypocenter. Figure 13 shows 1 s snapshots of the rupture, the main pulse of slip is directed northward and updip while there is a secondary, smaller pulse of slip that moves directly updip of the hypocenter then propagates north along the surface. Slip on the shallow northern segment of the fault occurs after the main rupture front has passed and suggests that this shallow slip has a delayed onset. Figure 14 shows the individual moment-rate functions for each subfault. The color underneath each curve is a reference rupture velocity. This indicates how quickly the rupture front would have to travel to reach the subfault at that particular instant in time. Most of the rupture occurs immediately following the main rupture front traveling at 3 km/s. Moment is released at the subfaults in the main asperity within 1 s of slip initiation. The shallowest subfaults (roughly down to 3–4 km) show longer durations of moment release with most of the slip occurring after the main rupture front moving at 3 km/s passes through them. The time evolution of slip can also be seen in Animation S1 where we plot slip rate as a function of time. Peak slip rate is ~ 3.4 m/s in the subfaults of the main asperity and slower (< 1.5 m/s) in the shallow subfaults. This is consistent with softer material rupturing at the surface. We tested a slip model with S wave rupture speed (3.3 km/s) and found slightly lower fits to the data (VR 68%).

In summary, it is important to note the improvement in the seismogeodetic source inversion over the GPS only insofar as a significant amount of deep slip now appears, bringing the solution closer to the final postprocessed solution. This has been seen in many joint source inversion results in continental environments [Wald and Heaton, 1994], namely, that GPS tends to capture the shallow slip while seismic

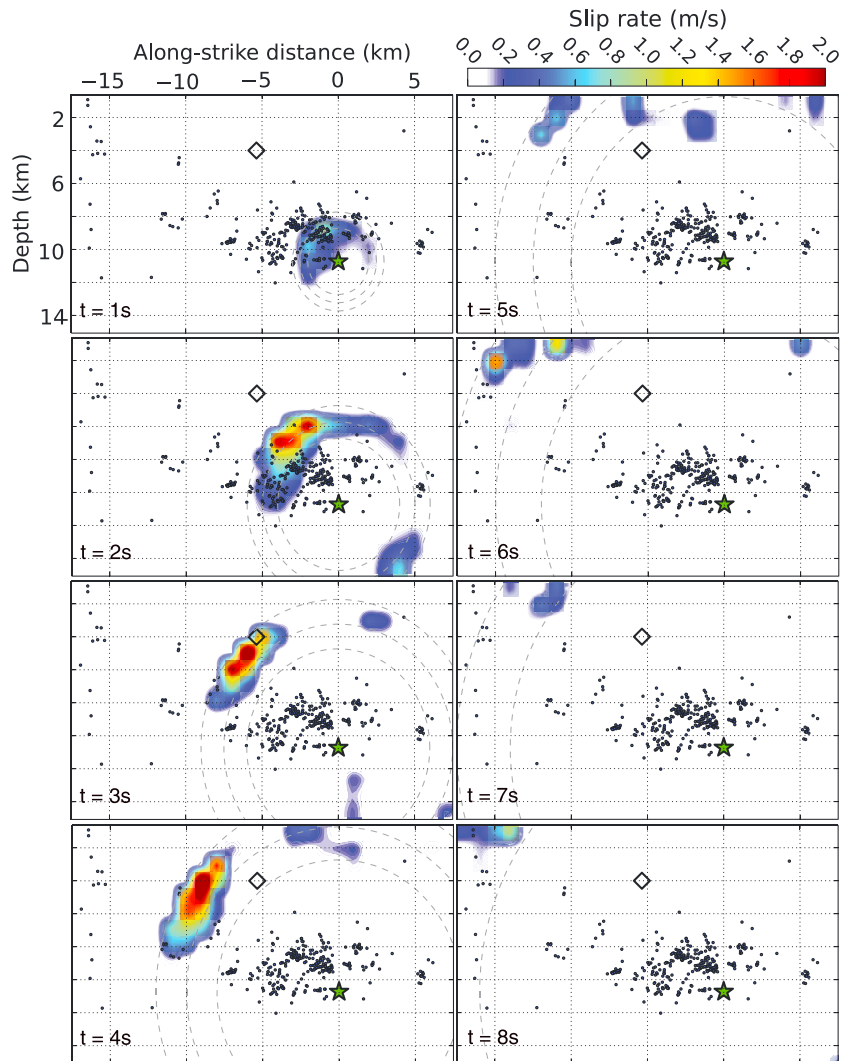


Figure 13. One second snapshots of rupture propagation for the joint inversion of Figure 12. The dotted concentric circles denote rupture propagating outward from the hypocenter (green star) at 2.0, 2.5, and 3.0 km/s. The black diamond is the location of the centroid computed from the postprocessed CMT inversion (Figure 7c). Black circles are the double difference relocated aftershocks.

data tend to capture the deep slip. Seismogeodetic data sets, even with the limited number of collocated sites in this case, provide this advantage. This is expected to have a significant impact on the ground motions and damage predicted in the near-source region.

4.7. Sensitivity Analysis

Using a procedure analogous to jackknife resampling, we can test the sensitivity of the postprocessed inversion to changes in the input data [Kim and Dreger, 2008] (Figure 15). First, we systematically test the sensitivity to the chosen distribution of seismogeodetic and strong motion stations. We remove one of the stations and rerun the inversion at the same regularization levels as the final inversion. We then reinsert that station into the inversion, remove another station, and rerun the inversion. We do this for every strong motion and seismogeodetic station. For the GPS-derived postprocessed daily coseismic offsets, we randomly select 20% of the offsets and remove them from the data set and rerun the inversion. We then reintroduce them and select another random 20% to remove. We repeat this process 30 times. Figure 15 shows the mean model, the standard deviation of the resampling, and the coefficient of variation (CV). The CV is the standard deviation normalized by the mean value of the model parameter.

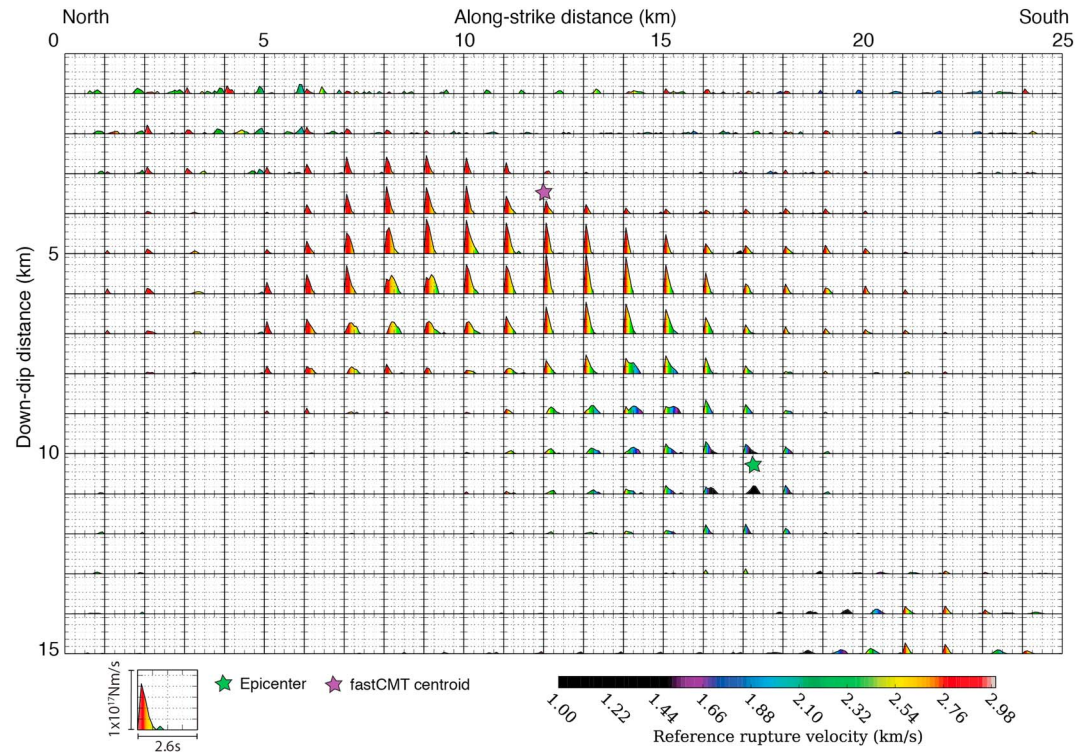


Figure 14. Subfault source time functions. The color underneath each curve is a reference rupture velocity. This indicates how quickly the rupture front would have to travel to reach the subfault at that particular instant in time.

The mean models are very similar to that shown in Figure 12. The coefficients of variation are low (<0.1) in the main asperity for both the seismogeodetic and strong motion, and GPS tests indicating that the feature is insensitive to the distribution of stations. Similarly, the shallow slip to the north and south has a low CV, indicating it is required to explain the data. There is a small patch in the shallow portion of the fault model, immediately updip of the centroid where the CV is ~ 0.8 . This suggests that perhaps the shallow slip is not continuous throughout the fault model and that perhaps there are two discrete patches of shallow slip, one to the north and one to the south of the centroid. Similarly, the patch of deep slip to the south and downdip of the hypocenter has a CV between 0.4 and 0.8, this indicates that its presence is inferred from data at only a few stations and it might not be a real feature. The high values of the CV in the areas where the mean model has little to no slip are to be expected. They reflect a significant variability in the model parameter (the amount of slip), but that the variability is around very small values of slip.

It is worth noting that the rapid kinematic solution with no positivity constraints is significantly smoother (Figure 11) than the postprocessed model (Figure 12) with positivity constraints. In both cases, the appropriate level of smoothing was selected from the ABIC using a nested grid of hyperparameters [Melgar and Bock, 2015]. Fukuda and Johnson [2008] found that when positivity is invoked, the ABIC solution might result in biased solutions. It is possible that this is reflected in our results. Other real-time approaches [Dreger et al., 2005] predefine the smoothing level; however ABIC, in spite of the potential bias studied by Fukuda and Johnson [2008], allows more flexibility and remains the most tractable technique for rapid computation. In supporting information Text S1 and Figure S1, there is further discussion on analysis of the resolution matrices for each data set. The joint resolution shows little along-strike structure; resolution mostly varies in the dip direction. There are no significant along-strike biases in the joint resolution matrix.

5. Discussion

We have presented results of a retrospective real-time analysis of GPS, seismic, and limited seismogeodetic data set available during the 2014 Napa earthquake (sections 4.1) and the rapid earthquake source

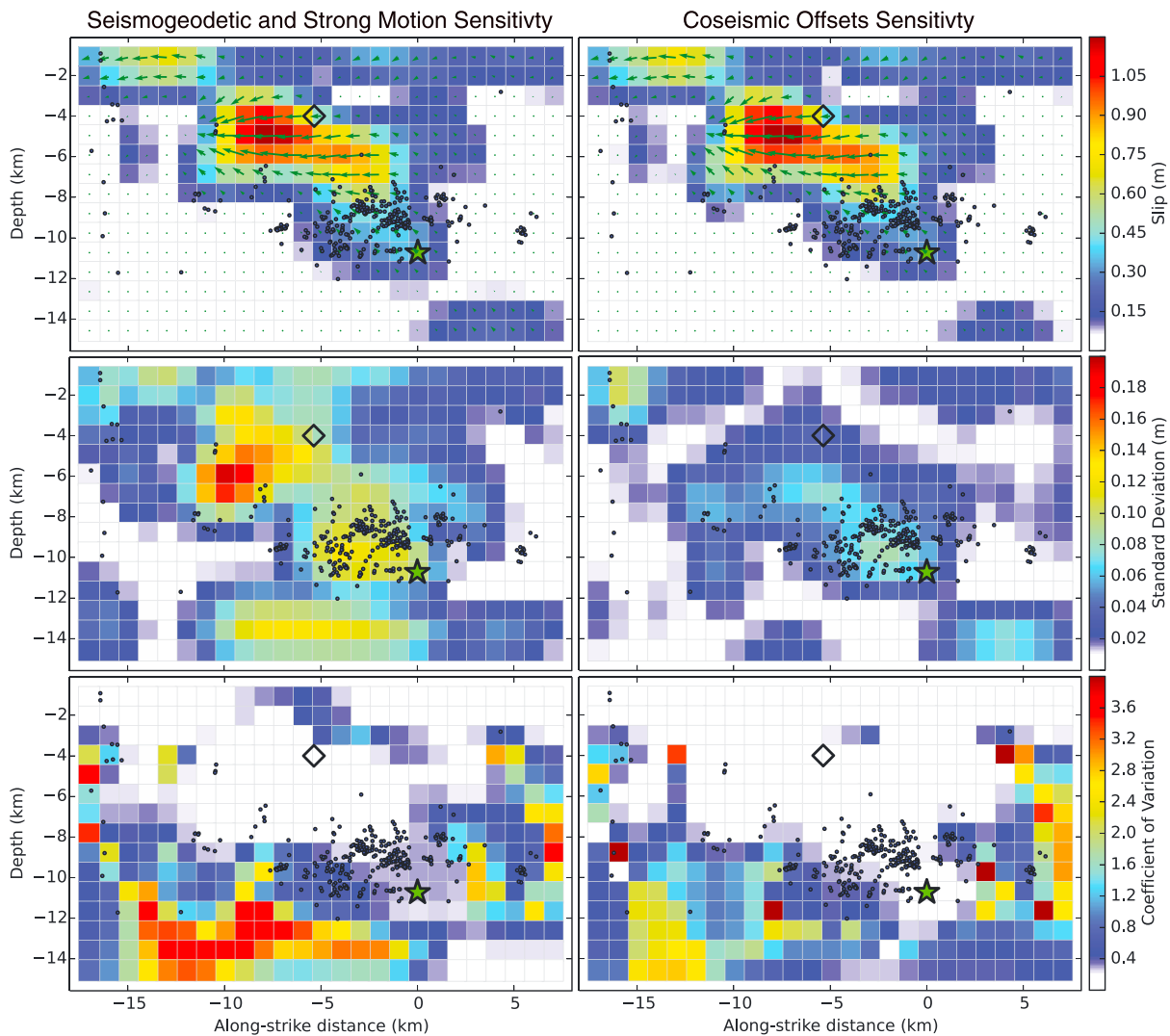


Figure 15. Jackknife sensitivity tests for the waveform data (seismogeodetic and strong motion) and coseismic offset data sets (see text for details). Plotted are the mean model, the standard deviation of the model parameters, and the coefficient of variation.

parameters derived from these data. This was followed by a rigorous postprocessed analysis of the data, some of which (i.e., postprocessed coseismic offsets) were not available until 48 h after the event, to better elucidate the static and kinematic characteristics of rupture (sections 4.6 and 4.7).

5.1. Rapid Response

There is now a significant body of research that argues for early warning and rapid response monitoring systems to include GPS data in some form [Crowell *et al.*, 2009]. Static offsets estimated from GPS measurements can provide rapid centroid moment tensors solutions and finite fault slip models to determine fault plane orientation and the geographic extent of rupture [Melgar *et al.*, 2012; Crowell *et al.*, 2012; Melgar *et al.*, 2013b; Minson *et al.*, 2014]. The prototype early warning system for California, with seismic data only [Bose *et al.*, 2014], identified the Napa event as magnitude $M_w 5.7$ within 3 s after OT. For this moderate event, there were not enough collocated GPS and seismic stations in the near-source region for the seismogeodetic waveforms to have significantly contributed to the early warning. The low station density might reflect that the perceived hazard was lower in the WNF, due to low-slip rate estimates (section 1), than for other parts of the plate boundary. Our retrospective real-time analysis of this event demonstrated that with the available station distributions, GPS can provide timely information to manage rapidly developing earthquake hazards. Using GPS-derived PGD-scaling relationships [Crowell *et al.*, 2013],

by 17 s after origin time (OT), four GPS stations had recorded significant displacements providing an initial estimate of M_w 5.6. By 20 s after OT, the PGD magnitude matched the early warning estimate (M_w 5.7). At 45 s after OT, the PGD-scaling relationships estimated an earthquake of a least M_w 6.0; by 50 s a CMT solution and finite fault static slip model could have been obtained, followed shortly thereafter by a kinematic source inversion of seismogeodetic data. The GlarmS prototype GPS warning system [Grapenthin *et al.*, 2014b] correctly identified the event and modeled it as a magnitude 5.8 to 5.9 earthquake by 80 s after OT. Both that system and the GPS-only results shown here (*fast*CMT and static slip inversion) are limited by the fact that the signal-to-noise ratio was not sufficiently high to correctly determine coseismic offsets at many affected stations that were subsequently resolved with postprocessed daily GPS displacements. The Napa earthquake with M_w 6.1 is just above the threshold [Geng *et al.*, 2013] at which near-source high-rate GPS time series (alone) begin to provide useful information to quickly model the earthquake source. This is evidenced by the centroid mislocation (Figure 7b) if the CMT is not first constrained to the hypocenter. Only four GPS stations in the region had offsets larger than 1.5 cm. This level was suggested by Melgar *et al.* [2012] as the threshold to include a GPS station into the CMT computation. The results shown here indicate that unless a substantial number of stations are significantly above this threshold, it is more reliable to constrain the CMT computation to the network-derived hypocenter as opposed to allowing a grid search for it. Nonetheless and in spite of these shortcomings, the nodal planes extracted from the CMT are useful for rapid static and kinematic source inversion.

An advantage of our GPS analysis approach is the use of the PPP-AR algorithm [Geng *et al.*, 2013] to estimate displacement waveforms. This does not require a reference station within the affected area. Furthermore, our approach does not require any prior assumptions on the earthquake mechanism, while a San Andreas-parallel fault structure was assumed in the operational system of Grapenthin *et al.* [2014b] to make the computation as quickly as possible. The real-time PPP-AR code we employed is undergoing extensive testing and its positions should be available soon. The postprocessed offsets, which have lower noise levels than the rapid ones, produce source models consistent with the kinematic postprocessed solution as well as with those found by other researchers. While the rapid offset *fast*CMT solution is less accurate than the postprocessed CMT, it does recover the correct nodal plane of the rupture, and the ensuing static slip inversion retrieves approximately the amount of slip, and indicates the extension of slip toward the surface as does the postprocessed solution. This indicates that the real-time offset accuracy is close to what is necessary to reliably image the source. Thus, it is important to understand why the rapid offsets fail to capture precisely some of the larger motions. A good example is station SVIN to the southwest of the epicenter (Figure S4). The north offset determined from the real-time positions is ~1 cm, but it is clear that there is a persistent long-period incremental trend in the data. In fact, a longer wait will produce larger (spurious) offsets. This is also particularly evident in the vertical direction. The postprocessed north offset for this site is 0.64 cm. This discrepancy is well within the noise levels of GPS, it affects the quality of the inversions given the small offsets, and reflects a fundamental limit of the applicability of real-time GPS for rapid modeling. The cause for these long-period drifts can be seen in Figures S5–S8 where we plot thousands of data for the four stations with the largest offsets for the day of the event, 24 August, and the preceding day. The time series for 23 August are shifted by 246 s to account for the sidereal period of the GPS orbits. We find that each of the four sites shows clear similarities between the 2 days, which means that long-period error is due to multipath effects inherent to the observation site.

While the static offsets for many sites are undetectable due to the low signal-to-noise ratio, the seismogeodetic solutions are still reliable. We have used the “loosely coupled” filter from Bock *et al.* [2011] where GPS positions are computed first and then combined with strong motion data. The “tightly coupled” alternative combines the strong motion and raw GPS observables [Geng *et al.*, 2013; Li *et al.*, 2013a, 2013b], although Geng *et al.* [2013] saw no substantial improvement in precision between the two approaches the tightly coupled filter may present advantages for the real-time implementation because of superior ambiguity resolution and more efficient throughput. The kinematic solution derived from the inversion of just the nine seismogeodetic stations contains many of the broad features of the final postprocessed solution that includes strong motion stations close to the source (which are difficult to use objectively in real time) and all postprocessed offsets. Recall that the advantage of the seismogeodetic waveforms is that they are not biased by baseline offsets in the accelerometer data and thus can be directly ingested into the kinematic inversion process without need for high-pass filtering. This is

appealing because the frequency band at which a particular accelerometer and channel will be reliable, or bias free is not known a priori. Thus, if kinematic modeling of the source is a goal of a particular geophysical network, then instrument collocation should be given a high priority. One possible solution is to incorporate low-cost MEMS accelerometers [Evans *et al.*, 2014] at GPS sites. Raw GPS telemetry requires a significantly greater bandwidth; thus, it would be preferable at instrument collocations to perform the seismogeodetic combination on site.

5.2. Source Kinematics and Surface Rupture

The postprocessed model of Figure 12 shows rupture predominantly to the north and updip of the hypocenter. The majority of moment release happens on the main asperity, 10 km in length with slip larger than 60 cm from 3 to 7 km depth and with a peak value of 1.2 m. Slip is fast and follows the main rupture front that propagates at the maximum allowed rupture speed of 3 km/s. This is roughly 90% of the shear wave speed. The relocated aftershock distribution is concentrated mostly to the north and updip of the hypocenter between 7 and 11 km depth. Interestingly, the region where most aftershocks occur has some slip (15–30 cm) implying that stress drop was only partial on this portion of the fault. There are no aftershocks on the main asperity, and there are very few aftershocks outside of the 7–11 km depth range. The shallow slip concentrated between 3 km and the surface appears continuous along strike throughout the model (although the sensitivity testing indicates that the portion immediately updip of the centroid might be spurious). It is possible then that there is one shallow patch of slip to the north of the centroid and another one to the south. The slip on the northern shallow patch occurs over a protracted period of time. This slower slip speed at shallow depths is consistent with rupture on softer layers with lower rigidities [Kanamori and Brodsky, 2004]. It is quite likely that 3-D propagation effects need to be taken into account to improve kinematic models of the event, particularly in the south where there are significant structures such as San Pablo Bay and the depth to the basement is variable [Graymer *et al.*, 2005]. Although peak amplitudes are well modeled, overall, stations to the south have poorer fits than those to the north of the event (Figure S10). We tested an inversion removing all of the southern strong motion stations and keeping only the northern ones located on class B sites. The results were mostly unaltered. This indicates that while 3-D GFs might introduce new, previously unmapped complexity into the source kinematics, at least the broad features of the rupture are persistent.

The surface trace of rupture exhibits significant complexity. In the soft sediments of Napa valley, there are two main strands of the surface rupture offset by roughly 2 km. Toward the north where the valley gives way to the Mayacama Mountains, the two strands join into a single fault, which correlates well with the previously assumed (UCERF3) location of the WNF [Field *et al.*, 2014]. The fault surface we have used throughout correlates well with the UCERF3 proposed location of the WNF and with the relocated aftershock cloud. All mapped surface features lie to the west of the intersection of the proposed fault plane and the surface. This suggests that the surface trace represents the expression of a secondary feature such as a flower structure, introduced into the soft sediments by the widespread shallow slip. For this interpretation, the location of the surface ruptures to the west of the main fault is mechanically consistent with a subvertical westward dipping strike-slip fault [Woodcock and Fischer, 1986; Woodcock and Rickards, 2003], where the secondary ruptures are all on the hanging wall of the dipping structure. This also suggests that a planar fault is only a first-order approximation. It is difficult to reconcile the western strands of surface rupture with the intersection of the fault plane with the free surface. This is the fault surface assumed by Dreger *et al.* [2015]. Indeed, if we force the inversion to a fault plane that starts at the western strand of rupture and crosses the aftershock distribution, the fits to the data, particularly the coseismic offsets, are reduced. This is not surprising since it was the coseismic offsets in the first place that constrained, via the CMT, the location of the slip surface. However, a westward dipping fault that surfaces at the eastern strand of the surface rupture is mechanically consistent. We tested such a model using a strike of 155° and a steeper dip of 79° and constraining the fault surface to go through the hypocenter. This fault trace constrained model (Figure 16) has larger moment (2.83×10^{19} Nm, M_w 6.21) than the original postprocessed solution (Figure 12). As with the original postprocessed model, it has one main asperity immediately to the northwest of the hypocenter albeit with smaller slip (~0.95 m). It also has a similar pattern of surface slip and total duration (~9.5 s). However, the source time function does not show the two moment-rate pulses and favors instead a steady moment release to a peak at 4 s. This fault trace constrained model also shows more widespread slip (<0.3 m) around the main asperity, whereas the original model in Figure 12 has no

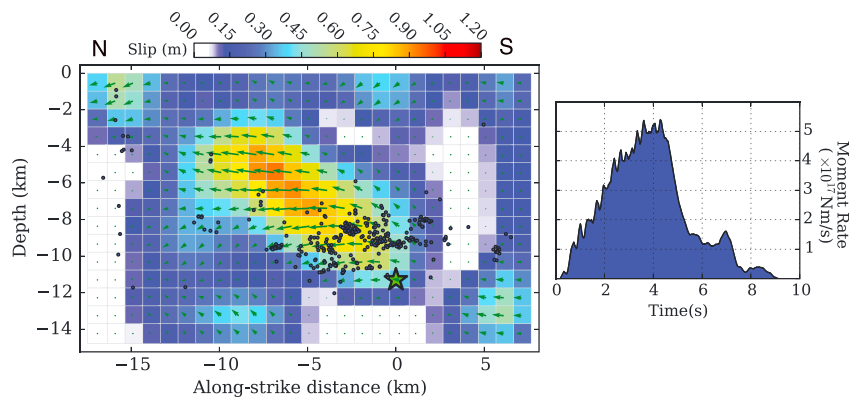


Figure 16. Slip distribution of the joint kinematic inversion of the nine seismogeodetic stations, 13 three-component strong motion stations, and daily coseismic offsets. This solution uses a fault plane constrained to match the easternmost strand of surface rupture (Figure 1b). The green star denotes the hypocenter. Black circles are the double difference relocated aftershocks. Moment release as a function of time for the event is shown at right.

slip downdip of the main asperity. This partly explains the larger moment and suggests more smearing and thus lower resolution on the surface trace constrained model. Figure 17 shows the surface projection of both models. The model that was forced to intersect the eastern surface trace fits the data (Figure S10) marginally worse (VR is 67%), although peak amplitudes remain well modeled. Thus, a model constrained to match the eastern surface trace seems plausible, and although it does not significantly improve data fits we cannot rule it out. We also see no evidence for an eastward dipping fault surface [Barnhart et al., 2015].

We posit that the fault surface trace reflects interactions with surface geology as it occurs only on the soft sedimentary cover of Napa valley and is absent in the mountains. Napa valley is overlain by a thick sedimentary layer [Graymer et al., 2005]. It is possible that the morphology of the surface trace is further

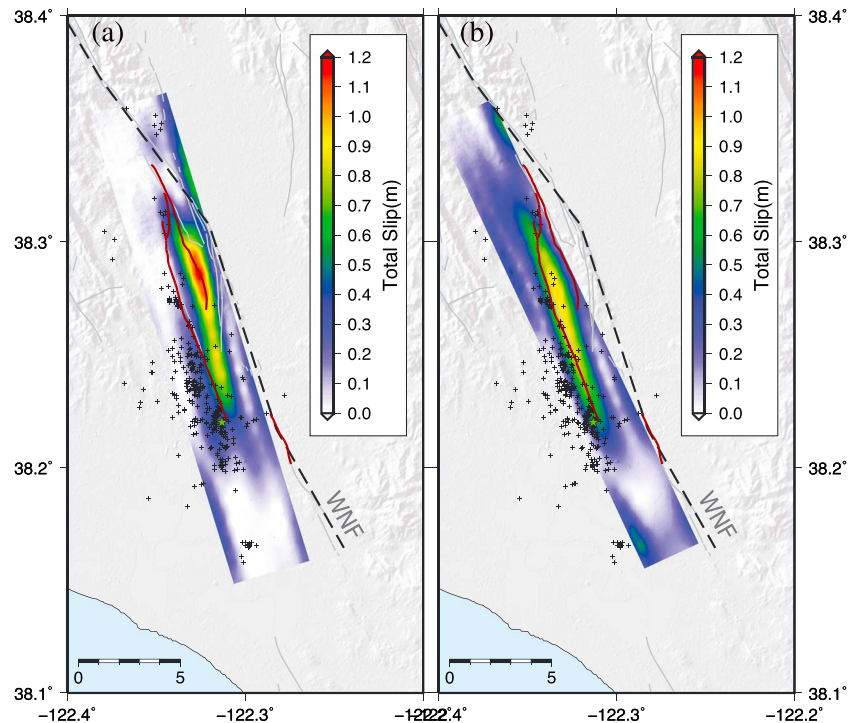


Figure 17. Map view of the projection of the slip distributions and their relationship to the surface rupture. (a) The inversion using the nodal plane from the postprocessed moment tensor (Figures 7c and 12) (b) The inversion constrained to match the easternmost strand of surface rupture (Figure 16).

controlled by the interaction of rupture with shallow geology and does not represent a direct extrapolation of the main dislocation surface at depth. This is evidenced by the behavior of the surface trace in the north where the western trace, as sediments thin and the rupture approaches the hills, progressively steps eastward eventually joining the eastern strand of the surface trace. InSAR scenes are decorrelated in the hills and thus cannot immediately resolve the location of the fault in this area. However, there are no known instances of surface rupture on bedrock for this event [Beyzaei *et al.*, 2014]. Additionally, numerical simulations show that for dipping faults the hanging wall will experience stronger shaking [Oglesby *et al.*, 2000; Oglesby and Day, 2001]. It is possible that some of the surface rupture features are also controlled by nonlinear behavior of the shallow layers subject to large ground motions. New measurements, such as from near-field lidar [Nissen *et al.*, 2012], will do much to elucidate the relation between slip at depth and the surface expression of rupture. If rupture was visible through the mountain core as, for example, in the El Mayor-Cucapah strike-slip event [Fletcher *et al.*, 2014], then perhaps it could be argued that the surface trace represents a more deep-seated process and an extrapolation of the fault geometry at depth. We find no evidence for this hypothesis and suggest instead that the surface trace reflects secondary structures in the sediment that should join the main dislocation surface at depth.

6. Conclusions

We have shown the potential contributions of real-time high-rate geodetic data to rapid earthquake response systems. We find that GPS-only data products such as PGD scaling, CMT computation, and static slip inversion can provide important first-look constraints on the characteristics of rupture independent of seismic network solutions. While the *fast*CMT solution for this event is limited by the higher noise levels in the real-time displacements, it does recover the correct nodal plane of the rupture. The ensuing static slip inversion retrieves approximately the amount of slip, and indicates the extension of slip toward the surface as in the postprocessed inversion. Furthermore, we have combined the GPS and strong motion data to retrospectively simulate the available seismogeodetic displacement and velocity waveforms that are free of systematic errors commonly found in GPS-only or seismic-only measurements of ground motion. We have shown that with current real-time infrastructure, this combination can produce a reliable kinematic source model. The improvement in the seismogeodetic source inversion over the GPS only is that a significant amount of deep slip now appears, bringing the solution closer to the final postprocessed solution. Seismogeodetic data sets, even with the limited number of collocated sites in this case, do provide this advantage. This is expected to have a significant impact on the ground motions, and thus damage, predicted in the near-source region. This study advances our knowledge significantly for the use of seismogeodetic data in the lower magnitude range, but is limited by the insufficient number and distribution of collocated sites.

Additionally, for post hoc detailed analysis of the source process, we have supplemented the seismogeodetic sites with strong motion sites close to the event and postprocessed static offset data. We found that if baseline offsets are suspected, treating acceleration data as velocity instead of displacement can minimize their effect. The postprocessed model reveals unilateral fast propagation, close to the shear wave speed of the assumed Earth model, with most of slip to the north of the hypocenter and a delayed onset of shallow slip. We have also argued that the observed surface ruptures are controlled by the shallow soft sediments of Napa valley and do not necessarily represent the intersection of the main faulting surface and the free surface. We tested a fault model that intersects the surface rupture and found that it provides comparable fit to the data. Regardless, our analysis suggests that the main dislocation plane should intersect the free boundary to the east either at the location of eastern strand of surface rupture or where the West Napa fault has been mapped in the past.

References

- Allen, T. I., and D. J. Wald (2009), On the use of high-resolution topographic data as a proxy for seismic site conditions (V_{S30}), *Bull. Seismol. Soc. Am.*, 99(2A), 935–943.
- Barnhart, W. D., J. R. Murray, S. H. Yun, J. L. Svarc, S. V. Samsonov, E. J. Fielding, and P. Milillo (2015), Geodetic constraints on the 2014 M_{6.0} South Napa earthquake, *Seismol. Res. Lett.*, 86(2A), 335–343.
- Beyzaei, C., et al. (2014), Geotechnical Engineering Reconnaissance of the August 24, 2014 M₆ South Napa earthquake, GEER Association Rep. GEER-037, 402 pp.

Acknowledgments

We thank UNAVCO for access to and maintenance of PBO high-rate GPS stations used in this study. BARD GPS data and BK seismic data are provided and maintained by the University of California Berkeley. NC seismic data are provided and maintained by the USGS and CE network seismic data by the California Geological Survey. We also thank Douglas Dreger, Arthur Rodgers, Valerie Sahakian, and Neal Driscoll for helpful discussions as well as Peter Lombard for assistance with v_{330} computations. We thank Xingxing Li and an anonymous reviewer for their constructive criticisms. This research was funded by the NASA Earth and Space Science Fellowship NNX12AN55H, NASA AIST-11 NNX09AI67G, ROSES NNX12AK24G, NSF EarthScope EAR-1252186, and NSF Instrumentation and Facilities EAR-1252187 awards. Additional funding for this work comes from the Gordon and Betty Moore Foundation through grant GBMF3024 to UC Berkeley. We thank the Nevada Geodetic Laboratory for their assistance. GPS data are available through UNAVCO data portal (<http://www.unavco.org/data/data.html>) and strong motion data through the Centre for Engineering Strong Motion (<http://strongmotioncenter.org/>). The postprocessed kinematic model is available in the supporting information, and codes used are available at <http://github.com/dmelgar>. The repository names are pykal for the Kalman filter, fastCMT for the moment tensor, and muddy for the static and kinematic slip inversion.

- Bock, Y., D. Melgar, and B. W. Crowell (2011), Real-time strong-motion broadband displacements from collocated GPS and accelerometers, *Bull. Seismol. Soc. Am.*, *101*(6), 2904–2925.
- Boore, D. M., and J. J. Bommer (2005), Processing of strong-motion accelerograms: Needs, options and consequences, *Soil Dyn. Earthquake Eng.*, *25*(2), 93–115.
- Bose, M., et al. (2014), Early warning for geological disasters, in *Early Warning for Geological Disasters, Advanced Technologies in Earth Sciences*, edited by F. Wenzel and J. Zschau, chap. 3, pp. 49–69, Springer, Berlin, doi:10.1007/978-3-642-12233-0.
- Cao, T., W. A. Bryant, B. Rowshandel, D. Branum, and C. J. Wills (2003), The revised 2002 California probabilistic seismic hazard maps, June 2003: California Geological Survey. [Available at http://www.consrv.ca.gov/CGS/rghm/psha/fault_parameters/pdf/2002_CA_Hazard_Maps.pdf.]
- Crowell, B. W., Y. Bock, and M. Squibb (2009), Demonstration of earthquake early warning using total displacement waveforms from real time GPS networks, *Seismol. Res. Lett.*, *80*(5), 772–782, doi:10.1785/gssrl.80.5.772.
- Crowell, B. W., Y. Bock, and D. Melgar (2012), Real-time inversion of GPS data for finite fault modeling and rapid hazard assessment, *Geophys. Res. Lett.*, *39*, L09305, doi:10.1029/2012GL051318.
- Crowell, B. W., D. Melgar, Y. Bock, J. S. Haase, and J. Geng (2013), Earthquake magnitude scaling using seismogeodetic data, *Geophys. Res. Lett.*, *40*, 6089–6094, doi:10.1002/2013GL058391.
- d'Alessio, M. A., I. A. Johanson, R. Bürgmann, D. A. Schmidt, and M. H. Murray (2005), Slicing up the San Francisco Bay Area: Block kinematics and fault slip rates from GPS-derived surface velocities, *J. Geophys. Res.*, *110*, B06403, doi:10.1029/2004JB003496.
- DeMets, C., R. G. Gordon, and D. F. Argus (2009), Geologically current plate motions, *Geophys. J. Int.*, *181*, 1–80, doi:10.1111/j.1365-246X.2009.04491.x.
- Dreger, D., and A. Kaverina (2000), Seismic remote sensing for the earthquake source process and near-source strong shaking: A case study of the October 16, 1999 Hector Mine earthquake, *Geophys. Res. Lett.*, *27*(13), 1941–1944, doi:10.1029/1999GL011245.
- Dreger, D., and B. Romanowicz (1994), Source characteristics of events in the San Francisco Bay Region, *U.S. Geol. Surv. Open File Rep.*, 94–176, 301–309.
- Dreger, D. S., L. Gee, P. Lombard, M. H. Murray, and B. Romanowicz (2005), Rapid finite-source analysis and near-fault strong ground motions: Application to the 2003 M_w 6.5 San Simeon and 2004 M_w 6.0 Parkfield earthquakes, *Seismol. Res. Lett.*, *76*(1), 40–48.
- Dreger, D. S., M. H. Huang, A. Rodgers, and K. Wooddell (2015), Kinematic finite-source model for the 24 August 2014 South Napa, California, earthquake from Joint Inversion of Seismic, GPS, and InSAR data, *Seismol. Res. Lett.*, *86*(2A), 327–334.
- Evans, E. L., J. P. Loveless, and B. J. Meade (2012), Geodetic constraints on San Francisco Bay Area fault slip rates and potential seismogenic asperities on the partially creeping Hayward fault, *J. Geophys. Res.*, *117*, B03410, doi:10.1029/2011JB008398.
- Evans, J. R., R. M. Allen, A. I. Chung, E. S. Cochran, R. Guy, M. Hellweg, and J. F. Lawrence (2014), Performance of several low-cost accelerometers, *Seismol. Res. Lett.*, *85*(1), 147–158.
- Field, E. H., R. J. Arrowsmith, G. P. Biasi, P. Bird, T. E. Dawson, K. R. Felzer, and Y. Zeng (2014), Uniform California Earthquake Rupture Forecast, Version 3 (UCERF3)—The time-independent model, *Bull. Seismol. Soc. Am.*, *104*(3), 1122–1180.
- Fletcher, J. M., O. J. Teran, T. K. Rockwell, M. E. Oskin, K. W. Hudnut, K. J. Mueller, and J. González-García (2014), Assembly of a large earthquake from a complex fault system: Surface rupture kinematics of the 4 April 2010 El Mayor–Cucapah (Mexico) M_w 7.2 earthquake, *Geosphere*, *10*(4), 797–827.
- Fukahata, Y., Y. Yagi, and M. Matsu'ura (2003), Waveform inversion for seismic source processes using ABIC with two sorts of prior constraints: Comparison between proper and improper formulations, *Geophys. Res. Lett.*, *30*(6), 1305, doi:10.1029/2002GL016293.
- Fukuda, J. I., and K. M. Johnson (2008), A fully Bayesian inversion for spatial distribution of fault slip with objective smoothing, *Bull. Seismol. Soc. Am.*, *98*(3), 1128–1146.
- Ge, M., G. Gendt, M. Rothacher, C. Shi, and J. Liu (2008), Resolution of GPS carrier-phase ambiguities in precise point positioning (PPP) with daily observations, *J. Geod.*, *82*(7), 389–399.
- Geng, J., F. N. Teferle, X. Meng, and A. H. Dodson (2011), Towards PPP-RTK: Ambiguity resolution in real-time precise point positioning, *Adv. Space Res.*, *47*(10), 1664–1673.
- Geng, J., Y. Bock, D. Melgar, B. W. Crowell, and J. S. Haase (2013), A new seismogeodetic approach applied to GPS and accelerometer observations of the 2012 Brawley seismic swarm: Implications for earthquake early warning, *Geochem. Geophys. Geosyst.*, *14*, 2124–2142, doi:10.1002/ggge.20144.
- Genrich, J. F., and Y. Bock (2006), Instantaneous geodetic positioning with 10–50 Hz GPS measurements: Noise characteristics and implications for monitoring networks, *J. Geophys. Res.*, *111*, B03403, doi:10.1029/2005JB003617.
- Grapenthin, R., I. A. Johanson, and R. M. Allen (2014a), Operational real-time GPS-enhanced earthquake early warning, *J. Geophys. Res. Solid Earth*, *119*, 7944–7965, doi:10.1002/2014JB011400.
- Grapenthin, R., I. Johanson, and R. M. Allen (2014b), The 2014 M_w 6.0 Napa earthquake, California: Observations from real-time GPS-enhanced earthquake early warning, *Geophys. Res. Lett.*, *41*, 8269–8276, doi:10.1002/2014GL061923.
- Graymer, R. W., D. A. Ponce, R. C. Jachens, R. W. Simpson, G. A. Phelps, and C. M. Wentworth (2005), Three-dimensional geologic map of the Hayward fault, northern California: Correlation of rock units with variations in seismicity, creep rate, and fault dip, *Geology*, *33*(6), 521–524.
- Holzer, T. L., A. C. Padovani, M. J. Bennett, T. E. Noce, and J. C. Tinsley (2005), Mapping NEHRP VS30 site classes, *Earthquake Spectra*, *21*(2), 353–370.
- Ide, S., M. Takeo, and Y. Yoshida (1996), Source process of the 1995 Kobe earthquake: Determination of spatio-temporal slip distribution by Bayesian modeling, *Bull. Seismol. Soc. Am.*, *86*(3), 547–566.
- Kanamori, H., and E. E. Brodsky (2004), The physics of earthquakes, *Rep. Prog. Phys.*, *67*(8), 1429.
- Kim, A., and D. S. Dreger (2008), Rupture process of the 2004 Parkfield earthquake from near-fault seismic waveform and geodetic records, *J. Geophys. Res.*, *113*, B07308, doi:10.1029/2007JB005115.
- Li, X., M. Ge, Y. Zhang, R. Wang, B. Guo, J. U. R. Klotz, J. Wickert, and H. Schuh (2013a), High-rate coseismic displacements from tightly integrated processing of raw GPS and accelerometer data, *Geophys. J. Int.*, *195*, 612–624, doi:10.1093/gji/ggt249.
- Li, X., M. Ge, X. Zhang, Y. Zhang, B. Guo, R. Wang, and J. Wickert (2013b), Real-time high-rate co-seismic displacement from ambiguity-fixed precise point positioning: Application to earthquake early warning, *Geophys. Res. Lett.*, *40*, 295–300, doi:10.1002/grl.50138.
- Melgar, D. (2014), Seismogeodesy and rapid earthquake and tsunami source assessment, PhD dissertation, 247 pp., Univ. of California, San Diego, Calif.
- Melgar, D., and Y. Bock (2015), Kinematic earthquake source inversion and tsunami inundation prediction with regional geophysical data, *J. Geophys. Res. Solid Earth*, *120*, doi:10.1002/2014JB011832.
- Melgar, D., Y. Bock, and B. W. Crowell (2012), Real-time centroid moment tensor determination for large earthquakes from local and regional displacement records, *Geophys. J. Int.*, *188*(2), 703–718.

- Melgar, D., Y. Bock, D. Sanchez, and B. W. Crowell (2013a), On robust and reliable automated baseline corrections for strong motion seismology, *J. Geophys. Res. Solid Earth*, *118*, 1177–1187, doi:10.1002/jgrb.50135.
- Melgar, D., B. W. Crowell, Y. Bock, and J. S. Haase (2013b), Rapid modeling of the 2011 M_w 9.0 Tohoku-oki earthquake with seismogeodesy, *Geophys. Res. Lett.*, *40*, 2963–2968, doi:10.1002/grl.50590.
- Minson, S. E., J. R. Murray, J. O. Langbein, and J. S. Gombert (2014), Real-time inversions for finite fault slip models and rupture geometry based on high-rate GPS data, *J. Geophys. Res. Solid Earth*, *119*, 3201–3231, doi:10.1002/2013JB010622.
- Nissen, E., A. K. Krishnan, J. R. Arrowsmith, and S. Saripalli (2012), Three-dimensional surface displacements and rotations from differencing pre-and post-earthquake LiDAR point clouds, *Geophys. Res. Lett.*, *39*, L16301, doi:10.1029/2012GL052460.
- Oglesby, D. D., and S. M. Day (2001), Fault geometry and the dynamics of the 1999 Chi-Chi (Taiwan) earthquake, *Bull. Seismol. Soc. Am.*, *91*(5), 1099–1111.
- Oglesby, D. D., R. J. Archuleta, and S. B. Nielsen (2000), The three-dimensional dynamics of dipping faults, *Bull. Seismol. Soc. Am.*, *90*(3), 616–628.
- Smalley, R. (2009), High-rate gps: How High do we need to go?, *Seismol. Res. Lett.*, *80*(6), 1054–1061.
- Topozada, T. R., J. H. Bennett, C. L. Hallstrom, and L. G. Youngs (1992), 1898 Mare Island earthquake at the southern end of the Rodger Creek Fault, in *Proceedings of the Second Conference on Earthquake Hazards in the Eastern San Francisco Bay Area, California Department of Conservation, Division of Mines and Geology (California Geological Survey), Spec. Publ.*, vol. 113, edited by G. Borchardt et al., pp. 385–392.
- Unruh, J. R., K. I. Kelson, and A. Barron (2002), Critical evaluation of the northern termination of the Calaveras fault, eastern San Francisco Bay area, California: Final Tech. Rep., U.S. Geol. Surv., National Earthquake Hazards Reduction Program Award Number 00-HQ-GR-0082, 72 pp., July.
- Wald, D. J., and T. H. Heaton (1994), Spatial and temporal distribution of slip for the 1992 Landers, California, earthquake, *Bull. Seismol. Soc. Am.*, *84*(3), 668–691.
- Waldhauser, F., and W. L. Ellsworth (2002), Fault structure and mechanics of the Hayward fault, California, from double-difference earthquake locations, *J. Geophys. Res.*, *107*(B3), 2054, doi:10.1029/2000JB000084.
- Wang, R., F. L. Martin, and F. Roth (2003), Computation of deformation induced by earthquakes in a multi-layered elastic crust—FORTRAN programs EDGRN/EDCMP, *Comput. Geosci.*, *29*(2), 195–207.
- Wells, D. L., and K. J. Coppersmith (1994), New empirical relationships among magnitude, rupture length, rupture width, rupture area, and surface displacement, *Bull. Seismol. Soc. Am.*, *84*(4), 974–1002.
- Wesling, J. R., and K. L. Hanson (2008), Mapping of the West Napa fault zone for input into the Northern California Quaternary Fault Database, Final Tech. Rep., U.S. Geol. Surv. External Award Number 05HQAG0002, 4 tables, 12 figures, 1 plate, 1 appendix, 34 pp.
- Woodcock, N. H., and M. Fischer (1986), Strike-slip duplexes, *J. Struct. Geol.*, *8*(7), 725–735.
- Woodcock, N. H., and B. Rickards (2003), Transpressive duplex and flower structure: Dent Fault System, NW England, *J. Struct. Geol.*, *25*(12), 1981–1992.
- Working Group on Northern California Earthquake Potential (1996), Database of potential sources for earthquakes larger than magnitude 6 in northern California, *U.S. Geol. Surv. Open File Rep.*, 96–705, 53 pp.
- Wu, C., M. Takeo, and S. Takeo (2001), Source process of the Chi-Chi earthquake: A joint inversion of strong motion data and global positioning system data with a multifault model, *Bull. Seismol. Soc. Am.*, *91*(5), 1128–1143.
- Zhu, L., and L. A. Rivera (2002), A note on the dynamic and static displacements from a point source in multilayered media, *Geophys. J. Int.*, *148*(3), 619–627.
- Zumberge, J. F., M. B. Heflin, D. C. Jefferson, M. M. Watkins, and F. H. Webb (1997), Precise point positioning for the efficient and robust analysis of GPS data from large networks, *J. Geophys. Res.*, *102*(B3), 5005–5017, doi:10.1029/96JB03860.